A&A 588, A93 (2016)
DOI: 10.1051/0004-6361/201527398

Astronomy & Astrophysics

New quasars behind the Magellanic Clouds. Spectroscopic confirmation of near-infrared selected candidates

Valentin D. Ivanov[1,2], Maria-Rosa L. Cioni[3,4,5], Kenji Bekki[6], Richard de Grijs[7,8,9], Jim Emerson[10], Brad K. Gibson[11], Devika Kamath[12], Jacco Th. van Loon[13], Andrés E. Piatti[14,15], and Bi-Qing For[6]

[1] European Southern Observatory, Ave. Alonso de Córdova 3107, Vitacura, Santiago, Chile
e-mail: vivanov@eso.org
[2] European Southern Observatory, Karl-Schwarzschild-Str. 2, 85748 Garching bei München, Germany
[3] Universität Potsdam, Institut für Physik und Astronomie, Karl-Liebknecht-Str. 24/25, 14476 Potsdam, Germany
[4] Leibniz-Institut für Astrophysik Potsdam, An der Sternwarte 16, 14482 Potsdam, Germany
[5] University of Hertfordshire, Physics Astronomy and Mathematics, College Lane, Hatfield AL10 9AB, UK
[6] ICRAR, M468, The University of Western Australia, 35 Stirling Hwy, 6009 Crawley, Western Australia, Australia
[7] Kavli Institute for Astronomy and Astrophysics, Peking University, Yi He Yuan Lu 5, Hai Dian District, 100871 Beijing, PR China
[8] Department of Astronomy, Peking University, Yi He Yuan Lu 5, Hai Dian District, 100871 Beijing, PR China
[9] International Space Science Institute-Beijing, 1 Nanertiao, Hai Dian District, 100190 Beijing, PR China
[10] School of Physics and Astronomy, Queen Mary University of London, Mile End Road, London E1 4NS, UK
[11] E.A. Milne Centre for Astrophysics, Department of Physics & Mathematics, University of Hull, Hull HU6 7RX, UK
[12] Instituut voor Sterrenkunde, K. U. Leuven, Celestijnenlaan 200D bus 2401, 3001 Leuven, Belgium
[13] Lennard-Jones Laboratories, Keele University, ST5 5BG, UK
[14] Observatorio Astronómico, Universidad Nacional de Córdoba, Laprida 854, 5000 Córdoba, Argentina
[15] Consejo Nacional de Investigaciones Científicas y Técnicas, Av. Rivadavia 1917, C1033AAJ, Buenos Aires, Argentina

Received 18 September 2015 / Accepted 19 October 2015

ABSTRACT

Context. Quasi-stellar objects (quasars) located behind nearby galaxies provide an excellent absolute reference system for astrometric studies, but they are difficult to identify because of fore- and background contamination. Deep wide-field, high angular resolution surveys spanning the entire area of nearby galaxies are needed to obtain a complete census of such quasars.
Aims. We embarked on a program to expand the quasar reference system behind the Large and the Small Magellanic Clouds, the Magellanic Bridge, and the Magellanic Stream that connects the Clouds with the Milky Way.
Methods. Hundreds of quasar candidates were selected based on their near-infrared colors and variability properties from the ongoing public ESO VISTA Magellanic Clouds survey. A subset of 49 objects was followed up with optical spectroscopy.
Results. We confirmed the quasar nature of 37 objects (34 new identifications): four are low redshift objects, three are probably stars, and the remaining three lack prominent spectral features for a secure classification. The bona fide quasars, identified from their broad emisison lines, are located as follows: 10 behind the LMC, 13 behind the SMC, and 14 behind the Bridge. The quasars span a redshift range from $z \sim 0.5$ to $z \sim 4.1$.
Conclusions. Upon completion the VMC survey is expected to yield a total of ∼1500 quasars with $Y < 19.32$ mag, $J < 19.09$ mag, and $K_s < 18.04$ mag.

Key words. surveys – infrared: galaxies – quasars: general – Magellanic Clouds

1. Introduction

Quasi–stellar objects (quasars) are active nuclei of distant galaxies undergoing episodes of strong accretion. Typically, the contribution from the host galaxy is negligible and they appear as point-like objects with strong emission lines. Quasar candidates are often identified by their variability, a method pioneered by Hook et al. (1994). The recent studies of Gallastegui-Aizpun & Sarajedini (2014), Cartier et al. (2015), and Peters et al. (2015), among others, brought the number of sampled objects up to many thousands. Precise space-based photometry was also used (the *Kepler* mission; Shaya et al. 2015). Gregg et al. (1996) reported a large quasar selection based on their radio properties (see also White et al. 2000; Becker et al. 2001). The radio selection has often been complemented with other wavelength regimes to sample dusty reddened objects (Glikman et al. 2012). Shanks et al. (1991) demonstrated that the quasars contribute at least a third of the X-ray sky background. The realization that they are powerful X-ray sources led to identification of a large number of faint quasars (e.g., Boyle et al. 1993; Hasinger et al. 1998, and the subsequent papers in these series). Modern X-ray missions continue to contribute to this field (Loaring et al. 2005; Nandra et al. 2005). More recently, the distinct mid–infrared properties of quasars have come to attention, mainly due to the work of Lacy et al. (2004). These properties have been exploited further by Stern et al. (2012), Assef et al. (2013), and Ross et al. (2015). Finally, multi-wavelength selections are becoming common (DiPompeo et al. 2015).

Quasars are easily confirmed from optical spectroscopy, aiming to detect broad hydrogen (Lyα 1216 Å, Hδ 4101 Å, Hγ 4340 Å, Hβ 4861 Å, Hα 6563 Å), magnesium (MgII 2800 Å), and carbon (CIV 1549 Å, CIII] 1909 Å) lines, as well as some

narrow forbidden lines of oxygen ([OII] 3727 Å, [OIII] 4959 Å, 5007 Å). These lines also help to derive the quasars' redshifts (e.g., Vanden Berk et al. 2001).

Quasars are cosmological probes and serve as background "lights" to explore the intervening interstellar medium, but they also are distant unmoving objects used to establish an absolute astrometric reference system on the sky. The smaller the measured proper motions (PMs) of foreground objects are, the more useful the quasars become – as is the case for nearby galaxies. Quasars behind these galaxies are hard to identify because of foreground contamination, the additional reddening inside the galaxies themselves (owing to dust), and the galaxies relatively large angular areas on the sky, which implies the need to carry out dedicated wide-field surveys, sometimes covering hundreds of square degrees. The Magellanic Clouds system is an extreme case where these obstacles are notably enhanced: the combined area of the two galaxies, the Magellanic Bridge, and the Stream that connects them with the Milky Way is at least two hundred square degrees; the significant depth of the Small Magellanic Cloud (SMC) along the line of sight (e.g., de Grijs & Bono 2015) aggravates the contamination and reddening issues.

Cioni et al. (2013) reviewed previous works aiming at discovering quasars behind the Magellanic Clouds: Blanco & Heathcote (1986), Dobrzycki et al. (2002, 2003b,a, 2005), Geha et al. (2003), Kozłowski & Kochanek (2009), Kozłowski et al. (2012, 2011), and Véron-Cetty & Véron (2010). In this study we add the latest installment of the Magellanic Quasar Survey (MQS) by Kozłowski et al. (2013), who increased the number of spectroscopically confirmed quasars behind the Large Magellanic Cloud (LMC) and SMC to 758, almost an order of a magnitude higher than before.

The optical surveys can easily miss or misclassify some quasars; near- and mid-infrared surveys are necessary to obtain more complete samples; ∼90% of the MQS quasar candidates were selected from mid-IR *Spitzer* observations (see also van Loon & Sansom 2015). This motivated us to search for quasars in the VISTA (Visual and Infrared Survey Telescope for Astronomy; Emerson et al. 2006) Survey of the Magellanic Clouds system (VMC; Cioni et al. 2011). The European Southern Observatory's (ESO) VISTA is a 4.1 m telescope located on Cerro Paranal; it is equipped with VIRCAM (VISTA InfraRed CAMera; Dalton et al. 2006), a wide-field near-infrared camera producing $\sim 1 \times 1.5\,\mathrm{deg}^2$ tiles[1] working in the 0.9–2.4 μm wavelength range. The VISTA data are processed with the VISTA Data Flow System (VDFS; Irwin et al. 2004; Emerson et al. 2004) pipeline at the Cambridge Astronomical Survey Unit[2]. The data products are available through the ESO archive or the specialized VISTA Science Archive (VSA; Cross et al. 2012).

The VMC is an ESO public survey, covering $184\,\mathrm{deg}^2$ around the LMC, SMC, and the Magellanic Bridge and Stream, down to $K_\mathrm{s} = 20.3$ mag ($S/N \sim 10$; Vega system) in three epochs in the Y and J-bands, and 12 epochs in the K_s-band, spread over at least a year. The main survey goal is to study the star formation history (Kerber et al. 2009; Rubele et al. 2012, 2015; Tatton et al. 2013) and the geometry (Ripepi et al. 2012a,b, 2014, 2015; Tatton et al. 2013; Moretti et al. 2014; Muraveva et al. 2014) of the system. Furthermore, the depth and angular resolution of the VMC survey has the potential to enable detailed studies of the star and cluster populations (Miszalski et al. 2011; Gullieuszik et al. 2012; Li et al. 2014; Piatti et al. 2014, 2015b,a), including PM measurements.

Cioni et al. (2014) measured the PM of the LMC from one $\sim 1.5\,\mathrm{deg}^2$ tile, comparing the VISTA and 2MASS (Two Micron All Sky Survey; Skrutskie et al. 2003) data over a time baseline of about ten years and from VMC data alone within a time span of ∼1 yr. They used ∼40 000 stellar positions and a reference system established by ∼8000 background galaxies. Similarly, Cioni et al. (2015), measured the PM of the SMC with respect to ∼20 000 background galaxies. Background galaxies are numerous, but they are extended sources, and their positions cannot be measured as accurately as the positions of point sources. This motivated us to persist with our search and confirmation of background quasars. The current paper reports spectroscopic follow-up observations of the VMC quasar candidates from a pilot study of only 7 out of the 110 VMC tiles, which were the only ones completely observed at the time of the search. The full-scale project intends to select for the first time quasar candidates in the near-infrared over the entire Magellanic system.

2. Sample selection

Cioni et al. (2013) derived selection criteria to identify candidate quasars based on the locus of 117 known quasars in a $(Y-J)$ versus $(J-K_\mathrm{s})$ color–color diagram, and their K_s-band variability behavior. The diagram was based on average magnitudes obtained from deep tile images created by the Wide Field Astronomy Unit (WFAU[3]) as part of the VMC data processing with version 1.3.0 of the VDFS pipeline. The sample selected for our study is based on these criteria and we refer the reader to Cioni et al. (2013) for details. Table 1 lists the VMC identification (Col. 1), right ascension α and declination δ (J2000; Cols. 2 and 3), magnitudes in the Y, J, and K_s-bands (Cols. 4, 6, and 8), respectively, and their associated photometric uncertainties (Cols. 5, 7, and 9) for each candidate, while Col. 10 shows the object identification (ID) used in the spectroscopic observations[4]. The last is composed of two parts: the first indicating the VMC tile and the second representing the sequential number of the object in the catalog of all sources in that tile; the letter g indicates that a source was classified as extended by the VDFS pipeline. Extended sources were included in our search to ensure that low redshift quasars with considerable contribution from the host galaxy will not be omitted. Their extended nature is marginal because they are dominated by the nuclei and because they are still useful for quasar absorption line studies.

The sixty-eight brightest candidates were selected to homogeneously sample seven VMC tiles where quasars had not yet been found. The total number of candidates can increase greatly if fainter objects are considered. Forty-nine of these were followed up spectroscopically. Some contamination from young stellar objects, brown dwarfs, planetary nebulae, and post-AGB stars is expected. Cioni et al. (2013) estimated that the total number of quasars with $Y < 19.32$ mag, $J < 19.09$ mag, and $K_\mathrm{s} < 18.04$ mag is 1200 behind the LMC, 400 behind the SMC, 200 behind the Bridge, and 30 behind the Stream. Figure 1 shows the location of all confirmed quasars from the MQS and

[1] Tiles are contiguous images that combine six pawprints taken in an offset pattern; pawprint is an individual VIRCAM pointing that generates a non-contiguous image of the sky because of the gaps between the 16 detectors. See Cioni et al. (2011) for details on the VMC observing strategy.

[2] http://casu.ast.cam.ac.uk/

[3] http://www.roe.ac.uk/ifa/wfau/

[4] For the ESO Science Archive users: in the headers of the raw data LMC 4_3 2050g was mislabeled as LMC 4_3 2450g.

Table 1. VMC quasar parameters (in order of increasing right ascension).

VMC ID	α (J2000) (h:m:s)	δ (d:m:s)	Y (mag)	σ_Y (mag)	J (mag)	σ_J (mag)	K_{K_S} (mag)	σ_{K_S} (mag)	Object ID
VMC J001806.53−715554.2	00:18:06.53	−71:55:54.2	18.236	0.015	17.933	0.014	16.392	0.012	SMC 5_2 206g
VMC J002014.74−712332.3	00:20:14.74	−71:23:32.3	19.115	0.025	18.613	0.022	17.014	0.017	SMC 5_2 213
VMC J002714.03−714333.6	00:27:14.03	−71:43:33.6	17.766	0.012	17.439	0.011	15.905	0.010	SMC 5_2 1003g
VMC J002726.28−722319.2	00:27:26.28	−72:23:19.2	19.318	0.029	18.794	0.024	17.140	0.019	SMC 5_2 1545g
VMC J002956.48−714638.1	00:29:56.48	−71:46:38.1	19.216	0.027	18.847	0.026	17.832	0.026	SMC 5_2 241
VMC J003430.32−715516.4	00:34:30.32	−71:55:16.4	18.774	0.021	18.350	0.019	17.341	0.021	SMC 5_2 211
VMC J003530.33−720134.5	00:35:30.33	−72:01:34.5	19.033	0.025	18.539	0.022	17.269	0.020	SMC 5_2 203
VMC J011858.84−740952.3	01:18:58.84	−74:09:52.3	19.102	0.024	18.694	0.021	17.477	0.021	SMC 3_5 82
VMC J011932.23−734846.6	01:19:32.23	−73:48:46.6	19.257	0.027	18.807	0.022	17.170	0.018	SMC 3_5 22
VMC J012036.83−735005.2	01:20:36.83	−73:50:05.2	18.749	0.020	18.414	0.018	17.471	0.021	SMC 3_5 24
VMC J012051.41−735305.1	01:20:51.41	−73:53:05.1	18.794	0.021	18.399	0.017	17.478	0.021	SMC 3_5 15
VMC J012513.11−740921.9	01:25:13.11	−74:09:21.9	19.583	0.034	19.036	0.025	17.023	0.017	SMC 3_5 29
VMC J013052.23−740549.0	01:30:52.23	−74:05:49.0	19.251	0.027	19.024	0.025	17.661	0.023	SMC 3_5 33
VMC J013056.05−733753.6	01:30:56.05	−73:37:53.6	18.637	0.019	18.349	0.017	17.172	0.018	SMC 3_5 18
VMC J025439.93−725532.9	02:54:39.93	−72:55:32.9	19.228	0.028	19.027	0.028	17.729	0.024	BRI 3_5 211
VMC J025706.20−732428.5	02:57:06.20	−73:24:28.5	17.807	0.012	17.452	0.011	16.537	0.013	BRI 3_5 33
VMC J025754.82−731049.7	02:57:54.82	−73:10:49.7	18.911	0.022	18.514	0.020	17.408	0.020	BRI 3_5 127
VMC J025803.19−732450.6	02:58:03.19	−73:24:50.6	18.862	0.022	18.565	0.021	17.235	0.018	BRI 3_5 38
VMC J030042.62−733951.5	03:00:42.62	−73:39:51.5	18.866	0.023	18.588	0.022	17.482	0.021	BRI 3_5 45
VMC J030123.10−725547.5	03:01:23.10	−72:55:47.5	18.929	0.023	18.705	0.023	17.676	0.023	BRI 3_5 137
VMC J030314.74−724331.6	03:03:14.74	−72:43:31.6	19.307	0.028	18.817	0.024	17.564	0.022	BRI 3_5 191
VMC J035146.41−733728.8	03:51:46.41	−73:37:28.8	18.184	0.014	17.952	0.015	16.910	0.015	BRI 2_8 2
VMC J035153.88−733629.4	03:51:53.88	−73:36:29.4	19.204	0.026	18.903	0.026	17.919	0.026	BRI 2_8 136
VMC J035221.71−732741.4	03:52:21.71	−73:27:41.4	19.507	0.032	19.038	0.027	17.309	0.019	BRI 2_8 6
VMC J035815.43−732736.8	03:58:15.43	−73:27:36.8	18.160	0.014	17.897	0.015	16.455	0.012	BRI 2_8 122
VMC J040131.58−741649.4	04:01:31.58	−74:16:49.4	18.710	0.019	18.285	0.018	17.254	0.018	BRI 2_8 16
VMC J040258.93−734720.6	04:02:58.93	−73:47:20.6	19.073	0.024	18.646	0.021	17.620	0.022	BRI 2_8 128
VMC J040615.05−740945.7	04:06:15.05	−74:09:45.7	19.830	0.039	19.500	0.037	17.777	0.024	BRI 2_8 197
VMC J045027.05−711822.9	04:50:27.05	−71:18:22.9	18.967	0.020	18.761	0.023	17.478	0.023	LMC 4_3 95
VMC J045628.63−714814.5	04:56:28.63	−71:48:14.5	19.418	0.026	18.965	0.027	17.317	0.020	LMC 4_3 86
VMC J045632.10−724527.3	04:56:32.10	−72:45:27.3	18.855	0.019	18.557	0.021	17.215	0.019	LMC 4_3 2050g
VMC J045702.44−715932.9	04:57:02.44	−71:59:32.9	19.744	0.033	19.356	0.036	17.741	0.026	LMC 4_3 1029g
VMC J045709.91−713231.0	04:57:09.91	−71:32:31.0	19.683	0.031	19.296	0.034	17.881	0.028	LMC 4_3 95g
VMC J045904.65−715339.1	04:59:04.65	−71:53:39.1	19.722	0.033	19.336	0.035	17.548	0.023	LMC 4_3 54
VMC J045928.96−724354.5	04:59:28.96	−72:43:54.5	19.061	0.021	18.682	0.023	17.110	0.018	LMC 4_3 2423g
VMC J050251.97−644239.4	05:02:51.97	−64:42:39.4	19.363	0.025	18.934	0.026	17.647	0.024	LMC 9_3 2414g
VMC J050315.54−645455.3	05:03:15.54	−64:54:55.3	18.842	0.018	18.578	0.021	17.307	0.020	LMC 9_3 2639g
VMC J050358.74−650548.1	05:03:58.74	−65:05:48.1	19.754	0.032	19.237	0.031	17.500	0.022	LMC 9_3 3107g
VMC J050401.47−644552.0	05:04:01.47	−64:45:52.0	19.152	0.022	18.771	0.023	17.509	0.022	LMC 9_3 2375g
VMC J050434.46−641844.5	05:04:34.46	−64:18:44.5	19.319	0.024	18.963	0.026	18.034	0.031	LMC 9_3 137
VMC J050603.46−645953.1	05:06:03.46	−64:59:53.1	19.426	0.025	19.098	0.028	17.629	0.024	LMC 9_3 2728g
VMC J051005.36−650834.8	05:10:05.36	−65:08:34.8	19.782	0.033	19.327	0.033	17.998	0.030	LMC 9_3 3314g
VMC J055355.54−655020.7	05:53:55.54	−65:50:20.7	19.781	0.037	19.234	0.031	17.833	0.026	LMC 8_8 376g
VMC J055419.46−655632.7	05:54:19.46	−65:56:32.7	19.301	0.026	18.887	0.025	17.917	0.028	LMC 8_8 422g
VMC J055705.98−653852.8	05:57:05.98	−65:38:52.8	19.071	0.022	18.756	0.023	17.640	0.023	LMC 8_8 341g
VMC J055831.11−655200.5	05:58:31.11	−65:52:00.5	19.507	0.030	18.956	0.026	17.610	0.023	LMC 8_8 655g
VMC J060052.97−654002.5	06:00:52.97	−65:40:02.5	19.149	0.023	18.742	0.023	17.790	0.025	LMC 8_8 208g
VMC J060216.83−670156.3	06:02:16.83	−67:01:56.3	18.498	0.015	18.282	0.017	17.055	0.017	LMC 8_8 119
VMC J060229.02−655848.1	06:02:29.02	−65:58:48.1	19.194	0.024	18.854	0.024	17.956	0.028	LMC 8_8 106

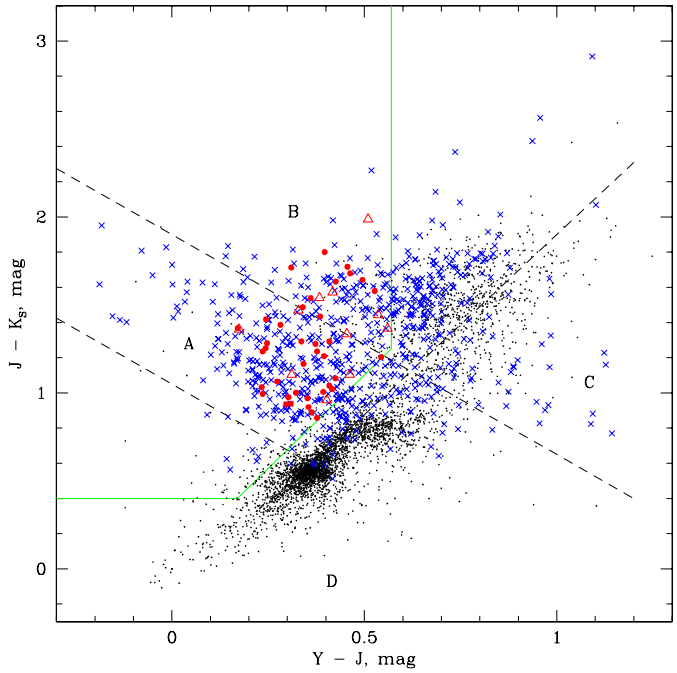

Fig. 1. Color–color diagram demonstrating the color selection of quasar candidates. The dashed black lines identify the regions (labeled with letters) where known quasars are found, while the green line marks the blue border of the planetary nebulae locus (Cioni et al. 2013). Our spectroscopically followed up quasars are marked with solid red dots, the non–quasars are marked with red triangles. Blue ×'s indicate the location of the VMC counterparts to the spectroscopically confirmed quasars from Kozłowski et al. (2013), selected adopting a maximum matching radius of 1 arcsec (the average separation is 0.15 ± 0.26 arcsec). Black dots are randomly drawn LMC objects (with errors in all three bands <0.1 mag) to demonstrate the locus of "normal" stars. Contaminating background galaxies are included among the black dots in regions B and C.

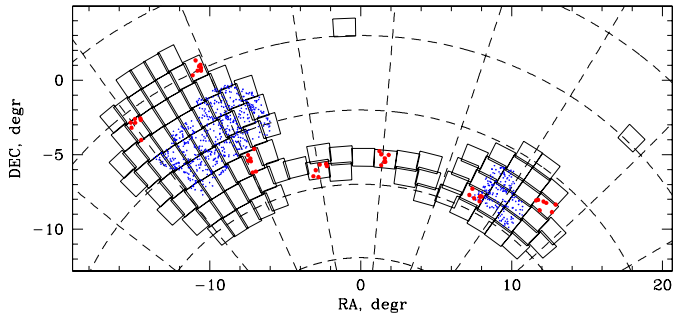

Fig. 2. Location of the spectroscopically followed up quasar candidates in this work (red) and confirmed quasars from Kozłowski et al. (2013) (blue). The VMC tiles are shown as contiguous rectangles. The dashed grid shows lines of constant right ascension (spaced by 15°) and constant declination (spaced by 5°). Coordinates are given with respect to $(\alpha_0, \delta_0) = (51°, -69°)$.

our candidates selected for follow-up spectroscopy in the $(Y-J)$ versus $(J-K_s)$ color–color diagram. A sky map showing our program objects is shown in Fig. 2, while Fig. A.1 depicts Y-band finding charts for all candidates. Most of our candidates are located in a sky area external to the OGLE III area studied by Kozłowski et al. (2013).

3. Spectroscopic follow-up observations

Follow-up spectra of 49 candidates were obtained with the FOcal Reducer and low dispersion Spectrograph (FORS2; Appenzeller et al. 1998) on the Very Large Telescope (VLT) in September−November 2013 in long-slit mode with the 300V+10 grism, GG435+81 order sorting filter, and 1.3 arcsec wide slit delivering spectra over $\lambda\lambda$ = 445–865 nm with a spectral resolving power $R = \lambda/\Delta\lambda \sim 440$. Two 450 s exposures were taken for most objects, except for some cases when the exposure time was 900 s. Occasionally, spectra were repeated because the weather deteriorated during the observations. We used some of the poor quality data, and a few objects objects ended up with more than two spectra. The signal-to-noise ratio varies across the spectra, but typically it is ∼10–30 at $\lambda \sim$ 6000–6200 Å. The observing details, including starting times, exposure times, starting and ending airmasses, and slit position angles for each exposure are listed in Table A.1. The reduced spectra are shown in Fig. 3.

The data reduction was carried out with the ESO pipeline, version 5.0.0. The spectrophotometric calibration was carried out with spectrophotometric standards (Oke 1990; Hamuy et al. 1992, 1994; Moehler et al. 2014a,b), observed and processed in the same manner as the program spectra. Various IRAF[5] tasks from the *onedspec* and *rv* packages were used in the subsequent analysis.

Quasar redshifts were measured in two steps. First, we visually identified the emission lines by comparing our spectra with the SDSS quasar composite spectrum (Vanden Berk et al. 2001). Given our wavelength coverage, if only one feature is visible, it is most likely MgII at $z \sim$ 1.1–1.3, otherwise another of the more prominent quasar lines would have to fall within the observed spectral range. Then, we measured the wavelengths of the features (mostly emission lines, but also some hydrogen absorption lines visible in the lower redshift objects), fitting them with a Gaussian profile using the IRAF task *splot*. This proved to be an adequate representation given the low resolution of our spectra. The lines, their observed wavelengths, and the derived redshifts are listed in Table A.1. Some emission lines were omitted if they fell near the edge of the wavelength range or if they were contaminated by sky emission lines and the sky subtraction left significant residuals. For most line centers the typical formal statistical errors are ∼1 Å and they translate into redshift errors of less than 0.001. These are optimistic estimates that neglect the wavelength calibration error. We evaluated these errors by measuring the wavelengths of 45 strong and isolated sky lines in five randomly selected spectra from our sample; we found no trends with wavelength and an rms of 1.57 Å. This translates into a redshift uncertainty of ∼0.0002 for a line at 7000 Å near the center of our spectral coverage.

To evaluate the real uncertainties we compared the redshifts derived from different lines of the same object (Fig. 4, top). The average difference for 35 pairs of lines is approximately zero: $\langle|z_i - z_j|\rangle = 0.006 \pm 0.007$. For objects with multiple lines we adopted the average difference as redshift error, adding in quadrature the wavelength calibration error of 0.0002. This addition only made a difference for a few low redshift objects. For quasars for which only a single line was available, we conservatively adopted a redshift error value of 0.005 for objects with $z < 1$ and 0.015 for the more distant ones.

[5] The Image Reduction and Analysis Facility is distributed by the National Optical Astronomy Observatory, which is operated by the Association of Universities for Research in Astronomy (AURA) under a cooperative agreement with the National Science Foundation.

Table 2. Derived parameters for the object in this paper.

Object ID	Spectral features and observed wavelength (Å)	Redshift z	Classification	Object ID	Spectral features and observed wavelength (Å)	Redshift z	Classification
SMC 5_2 206g	Hγ 7050.68 ± 1.51, Hβ 7890.34 ± 0.24, [OIII] 7993.89 ± 0.28, [OIII] 8118.30 ± 0.26	0.620 ± 0.006	quasar	BRI 2_8 136	CIV 5602.96 ± 5.95	2.617 ± 0.015	quasar
				BRI 2_8 6	MgII 6201.85 ± 3.99	1.216 ± 0.015	quasar
				BRI 2_8 122	MgII 5976.94 ± 0.42	1.136 ± 0.015	quasar
				BRI 2_8 16	CIII] 5183.56 ± 1.88	1.716 ± 0.015	quasar
SMC 5_2 213	MgII 6128.54 ± 1.71	1.190 ± 0.015	quasar	BRI 2_8 128	CIII] 5009.91 ± 1.12, MgII 7369.76 ± 0.45	1.629 ± 0.008	quasar
SMC 5_2 1003g	Hδ 6046.51 ± 0.64, Hγ 6403.86 ± 0.41, Hβ 7165.82 ± 0.24	0.474 ± 0.001	quasar	BRI 2_8 197	CIV 4808.12 ± 0.90, CIII] 5912.40 ± 1.53	2.101 ± 0.006	quasar
SMC 5_2 1545g	MgII 4751.83 ± 0.05, Hβ 8249.33 ± 0.09 [OIII] 8496.75 ± 0.06	0.697 ± 0.001	quasar	LMC 4_3 95	Hα 6568.75 ± 0.06	0.001 ± 0.005	star
				LMC 4_3 86	Hα 6566.98 ± 0.17, Hβ 4865.29 ± 0.49	0.0004 ± 0.0003	star
SMC 5_2 241	SiIV 7129.73 ± 1.63, CIV 7887.25 ± 1.61	4.098 ± 0.013	quasar	LMC 4_3 2050g	CIV 4716.14 ± 0.44, CIII] 5808.61 ± 1.65, MgII 8553.64 ± 5.60	2.048 ± 0.007	quasar
SMC 5_2 211	CIII] 5452.33 ± 3.50, MgII 8011.68 ± 2.19	1.860 ± 0.006	quasar	LMC 4_3 1029g	poor quality	–	unknown
SMC 5_2 203	[OIII] 8088.58 ± 2.39	0.667 ± 0.015	quasar	LMC 4_3 95g	MgII 6249.31 ± 0.30	1.233 ± 0.015	quasar
SMC 3_5 82	CIV 6200.63 ± 1.10	3.003 ± 0.015	quasar	LMC 4_3 54	CIII] 5903.83 ± 0.84, MgII 8661.03 ± 2.31	2.094 ± 0.002	quasar
SMC 3_5 22	CIII] 5999.83 ± 1.22	2.143 ± 0.015	quasar				
SMC 3_5 24	CIII] 5371.40 ± 1.23, MgII 7913.45 ± 3.23	1.821 ± 0.013	quasar	LMC 4_3 2423g	MgII 5629.43 ± 0.16	1.011 ± 0.015	quasar
				LMC 9_3 2414g	MgII 6675.13 ± 0.96	1.385 ± 0.015	quasar
SMC 3_5 15	CIII] 4839.23 ± 2.87, MgII 7137.49 ± 0.44	1.543 ± 0.015	quasar	LMC 9_3 2639g	CIV 5133.74 ± 0.88, CIII] 6315.68 ± 3.13	2.311 ± 0.005	quasar
SMC 3_5 29	Hα 6567.83 ± 0.01, Hβ 4863.61 ± 0.67	0.0003 ± 0.0004	star	LMC 9_3 3107g	no lines	–	unknown
				LMC 9_3 2375g	MgII 6299.72 ± 1.17	1.251 ± 0.015	quasar
SMC 3_5 33	CIV 033.41 ± 1.03, CIII] 6195.82 ± 3.31	2.248 ± 0.003	quasar	LMC 9_3 137	CIII] 5679.54 ± 2.52, MgII 8375.65 ± 1.57	1.984 ± 0.017	quasar
SMC 3_5 18	MgII 6622.75 ± 0.99	1.366 ± 0.015	quasar	LMC 9_3 2728g	Hβ 7344.57 ± 0.07, [OIII] 7491.30 ± 0.03, [OIII] 7564.71 ± 0.01	0.510 ± 0.001	galaxy
BRI 3_5 211	CIII] 5452.33 ± 3.50, MgII 8011.68 ± 2.19	2.078 ± 0.012	quasar				
BRI 3_5 33	CIII] 5067.02 ± 2.14, MgII 7446.36 ± 0.67	1.658 ± 0.006	quasar	LMC 9_3 3314g	no lines	–	unknown
				LMC 8_8 376g	poor quality	–	unknown
BRI 3_5 127	CIII] 4929.99 ± 2.13, MgII 7258.02 ± 1.32	1.588 ± 0.010	quasar	LMC 8_8 422g	no lines	–	unknown
				LMC 8_8 341g	Hα 6573.06 ± 3.54	0.001 ± 0.005	galaxy
BRI 3_5 38	MgII 6533.03 ± 1.71	1.334 ± 0.015	quasar	LMC 8_8 655g	Hβ 6958.04 ± 0.05, [OIII] 7099.11 ± 0.36, [OIII] 7166.94 ± 0.16	0.431 ± 0.001	galaxy
BRI 3_5 45	CIII] 5147.57 ± 0.99	1.697 ± 0.015	quasar				
BRI 3_5 137	CIII] 5609.65 ± 4.06, MgII 8265.13 ± 2.15	1.946 ± 0.014	quasar				
				LMC 8_8 208g	Hβ 5306.51 ± 0.05, [OIII] 5412.67 ± 0.21, [OIII] 5465.28 ± 0.08, Hα 7163.06 ± 0.07	0.0912 ± 0.0003	galaxy
BRI 3_5 191	SiIV 6004.60 ± 1.31, CIV 6651.75 ± 3.87	3.297 ± 0.005	quasar				
BRI 2_8 2	SiIV 4877.55 ± 1.46, CIV 5374.87 ± 1.36, CIII] 6622.25 ± 9.14	2.477 ± 0.022	quasar	LMC 8_8 119	MgII 6128.07 ± 0.20	1.190 ± 0.015	quasar
				LMC 8_8 106	CIII] 5161.41 ± 2.87	1.704 ± 0.015	quasar

Notes. Detected spectral features and their central wavelengths, estimated redshifts, and the object classifications are listed.

Finally, as external verification we re–measured in the rest–frame SDSS composite spectrum the redshifts of the same lines that were detected in our spectra, obtaining values below 0.0001, as expected.

4. Results

The majority of the observed objects are quasars: 37 objects (in the first four panels of Fig. 3) appear to be bona fide quasars

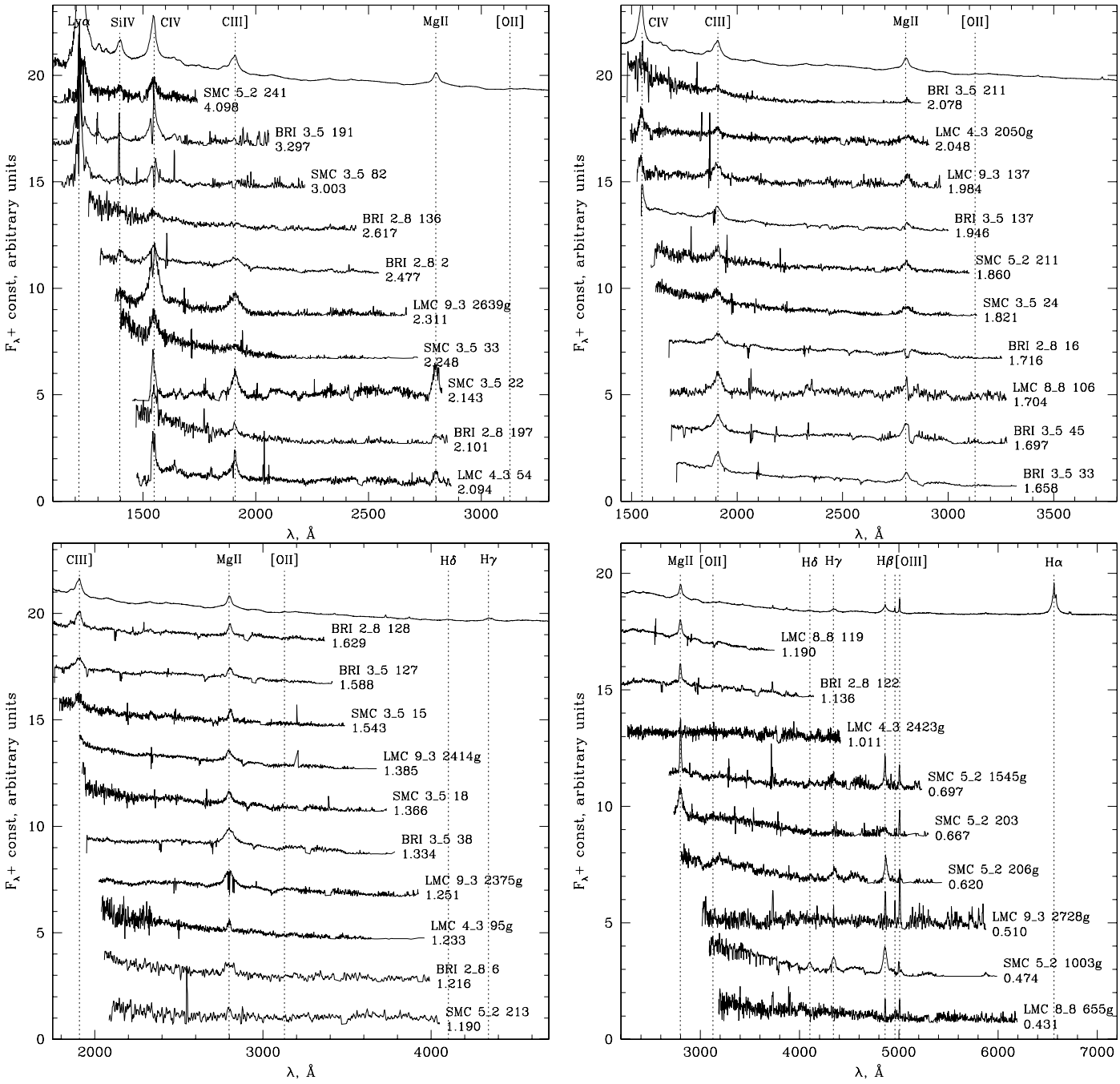

Fig. 3. Spectra of the quasar candidates sorted by redshift and shifted to rest-frame wavelength. The spectra were normalized to an average value of one and shifted vertically by offsets of two, four, etc., for display purposes. The SDSS composite quasar spectrum (Vanden Berk et al. 2001) is shown at *the top of all panels*. A sky spectrum is shown at *the bottom of the fifth panel* (see the next page). Objects with no measured redshift due to lack of lines or low signal-to-noise are plotted assuming $z = 0$ in the fifth panel next to the sky spectrum to facilitate the identification of the residuals from the sky emission lines.

at $z \sim 0.47$–4.10; they show some broad emission lines even though some spectra need smoothing (block averaging, typically by 4−8 resolution bins) for display purposes. The spectra of the three highest redshift quasars show Lyα absorption systems; a few quasars (e.g., SMC 3_5 22, BRI 2_8 197, etc.) show blueshifted CIV absorption (Fig. 3, panel 1), perhaps due to an AGN wind. We defer more detailed study of individual objects until the rest of the sample has been followed up.

These objects are marked in the last column of Table A.1 as quasars: 10 are behind the LMC, 13 behind the SMC, and 14 behind the Bridge area. The VDFS pipeline classified 28 of the confirmed quasars as point sources and 9 as extended (recognizable by the "g" in their names). This does not necessarily mean that the VISTA data resolved their host galaxies since the extended sources are uniformly spread over the redshift range – about half of them have $z \sim 1$–2 – and random alignment with objects in the Magellanic Clouds can easily affect their appearance. Our success rate is ~76%, testifying to the robustness and reliability of our selection criteria. There are more candidates that turned out not to be quasars in region B than in region A of

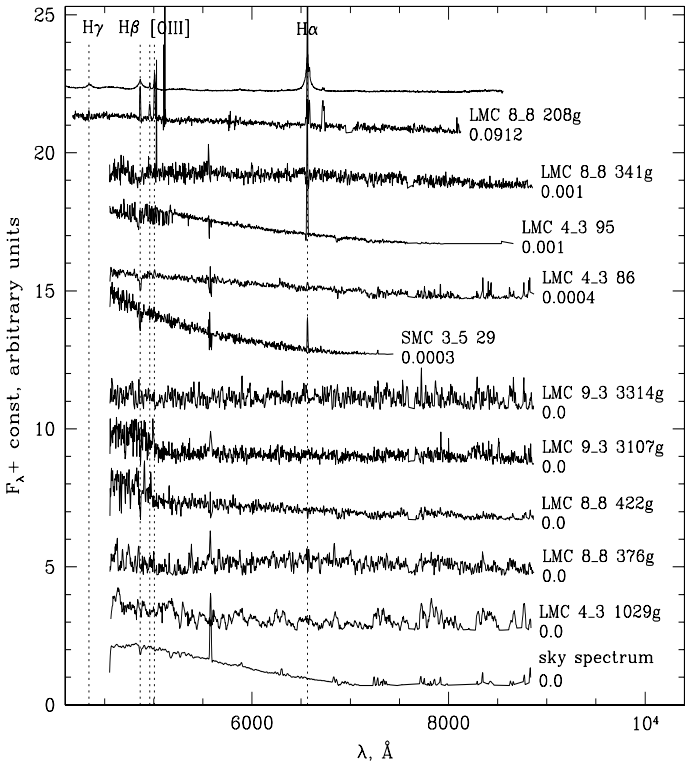

Fig. 3. continued.

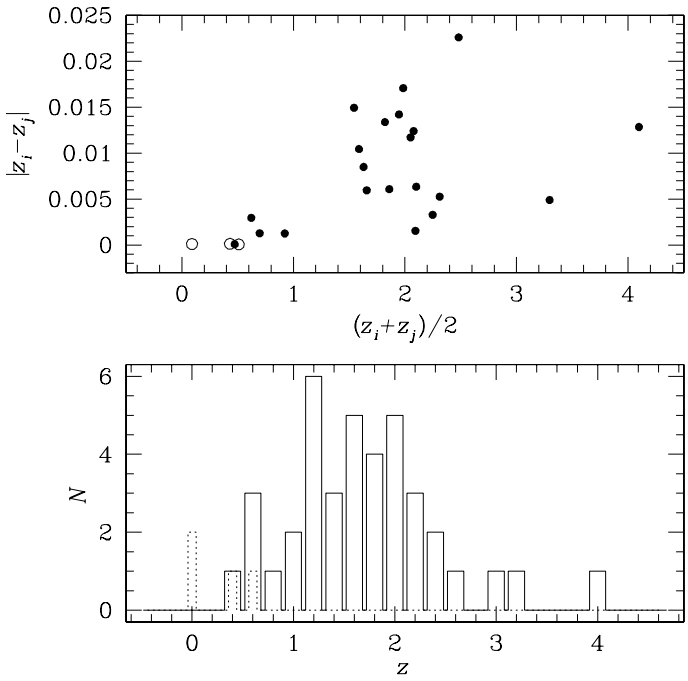

Fig. 4. *Top*: differences between redshifts z_i and z_j derived from each available pair of lines i and j for objects with multiple lines for bona fide quasars (solid dots) and galaxies (circles). *Bottom*: redshift histogram for 47 objects in our sample with reliably detected emission lines for bona fide quasars (solid line) and galaxies (dashed line).

the color–color diagram (see Fig. 1), but for now our statistical basis is small; a follow up of more candidates is needed to draw any definitive conclusion.

The majority of quasars with redshift $z \leq 1$ were classified as extended sources by the VDFS pipeline, supporting our decision to include extended objects in the sample. Four extended objects are contaminating low redshift galaxies: LMC 9_3 2728g, LMC 8_8 655g, and LMC 8_8 208g show hydrogen, some oxygen, and nitrogen in emission, but no obvious broad lines, so we interpret these as indicators of ongoing star formation rather than nuclear activity, while LMC 8_8 341g may also show Hβ in absorption. Furthermore, LMC 8_8 341g has a recession velocity of $\sim$300 km s^{-1}, consistent within the uncertainties with LMC membership ($V_{\rm rad}$ = 262.2 ± 3.4 km s^{-1}, McConnachie 2012), which makes it a possible moderately young LMC cluster. The spectra of all these objects are shown in Fig. 3, panel 5.

Three point–source–like objects are most likely emission line stars: LMC 4_3 95, LMC 4_3 86, and SMC 3_5 29. These spectra are also shown in Fig. 3, panel 5.

The spectra of LMC 8_8 422g, LMC 4_3 3314g, and LMC 9_3 3107g (Fig. 3, panel 5) offer no solid clues as to their nature. Some BL Lacertae – active galaxies believed to be seen along a relativistic jet coming out of the nucleus – are also featureless, but they usually have bluer continua than the spectra of these three objects (Landoni et al. 2013)[6]. A possible test is to search for rapid variability, typical of BL Lacs, but the VMC cadence is not well suited for such an exercise, and the light curves of the three objects show no peculiarities. Finally, the spectra of LMC 4_3 1029g and LMC 8_8 376g (Fig. 3, panel 5) are too noisy for secure classification. The spectra of the five objects with no classification are plotted in the last panel in Fig. 3 at redshifts $z = 0$ to facilitate easier comparison with the sky spectrum shown just below them.

After target selection we realized that three of our candidates were previously confirmed quasars, and two more were suspected to be quasars. Tinney et al. (1997) selected SMC 5_2 203 (their designation [TDZ97] QJ0035−7201 or SMC-X1-R-4; our spectrum is plotted in Fig. 3, panel 4) from unpublished ROSAT SMC observations. They confirmed it spectroscopically and estimated a redshift of z = 0.666 ± 0.001, in excellent agreement with our value of z = 0.667 ± 0.015. Kozłowski et al. (2013) identified SMC 3_5 24 and SMC 3_5 15 (Fig. 3, panels 2 and 3, respectively) and reported spectroscopic confirmation of their quasar nature, measuring redshifts of z = 1.820 and z = 1.549, respectively, also very similar to our values of z = 1.821 ± 0.013 and z = 1.543 ± 0.015. LMC 9_3 137 and LMC 4_3 95g were listed as AGN candidates by Kozłowski & Kochanek (2009): [KK2009] J050434.46−641844.4 and [KK2009] J045709.93−713231.0 based on their mid-infrared colors (Fig. 3, panels 2 and 3, respectively).

The ROSAT all-sky survey (Voges et al. 1999) reported an X-ray source at a separation of 7″ from our estimated position of the confirmed quasar LMC 8_8 119 (Fig. 3, panel 4). Flesch (2010) associated the X-ray source with a faint object on the Palomar Observatory Sky Survey, but estimated 50% probability that this is a random alignment, and only 17% that the X-ray emission originates from a quasar.

Many of our quasars are present in the GALEX (Galaxy Evolution Explorer; Morrissey et al. 2007) source catalog, and in the SAGE–SMC (Surveying the Agents of Galaxy Evolution – Small Magellanic Cloud; Gordon et al. 2011) source catalog. The confirmed quasar SMC 5_2 241 (Fig. 3, panel 1) stands out; in addition to the GALEX and SAGE detections, it has a candidate radio counterpart: SUMSS J002956−714640 at 2.8 arcsec

[6] Spectral library: http://archive.oapd.inaf.it/zbllac/

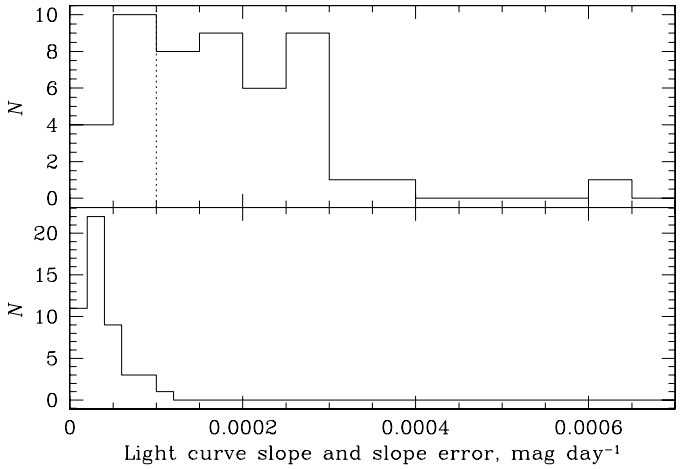

Fig. 5. Histograms of the slope variations (*top*; the vertical dashed line shows the slope variation limit of 0.0001 mag day^{-1}, adopted in our quasar selection) and the slope uncertainties (*bottom*) for linear fits to the light curves of the objects in our sample.

separation from the 843 MHz Sydney University Molonglo Sky Survey (Bock et al. 1999; Mauch et al. 2003).

We revised the light curves of our observed objects because a larger number of K_s-band measurements have become available since the target selection in Cioni et al. (2013), allowing us to investigate further the near-infrared variability properties of the quasars. Light curves based on all individual pawprint measurements from all processed data at CASU as of March 2015 for all our objects are shown in Fig. A.2. We applied the same variability parameterization with the slope of a linear fit to the light curve, as in Cioni et al. (2013). The distribution of absolute slope values (i.e., slope variation) shows a dip corresponding to flat light curves, which corresponds to our criterion to select variable sources with slope variation >0.0001 mag day^{-1} (Fig. 5). The additional data have moved some of the selected quasars into the low-variation zone.

Cioni et al. (2013) estimated that the VMC survey will find in total about 1830 quasars. The success rate of 76% reached in this paper brings this number down to about 1390. The spectra of the candidates in 7 tiles out of the 110 tiles that comprise the entire VMC survey yielded on average ~5.3 quasars per tile. Scaling this number up to the full survey area yields ~580 quasars. This is a lower limit because only the brightest candidates in the seven tiles were followed up, so the larger number is still a viable prediction.

5. Summary

We report spectroscopic follow-up observations of 49 quasar candidates selected based on their colors and variability. They are located behind the LMC, SMC, and the Bridge area connecting the Clouds: 37 of these objects are bona fide quasars of which 34 are new discoveries. Therefore, the success rate of our quasar search is ~76%. The project is still at an early stage, but once the spectroscopic confirmation has been obtained, the identified quasars will provide an excellent reference system for detailed astrometric studies of the Magellanic Cloud system. Furthermore, the homogeneous multi-epoch observations of the VMC survey, together with the large quasar sample, open up the possibility of investigating in detail the mechanisms that drive quasar variability, for example, with structure functions in the near-infrared, following the example of the SDSS quasar variability studies (e.g., Vanden Berk et al. 2004).

Acknowledgements. This paper is based on observations made with ESO telescopes at the La Silla Paranal Observatory under program ID 092.B-0104(A). We have made extensive use of the SIMBAD Database at CDS (Centre de Données astronomiques) Strasbourg, the NASA/IPAC Extragalactic Database (NED) which is operated by the Jet Propulsion Laboratory, CalTech, under contract with NASA, and of the VizieR catalog access tool, CDS, Strasbourg, France. R.d.G. acknowledges funding from the National Natural Science Foundation of China (grant 11373010). We thank the anonymous referee for the comments that helped to improve the paper.

References

Appenzeller, I., Fricke, K., Fürtig, W., et al. 1998, The Messenger, 94, 1
Assef, R. J., Stern, D., Kochanek, C. S., et al. 2013, ApJ, 772, 26
Becker, R. H., White, R. L., Gregg, M. D., et al. 2001, ApJS, 135, 227
Blanco, V. M., & Heathcote, S. 1986, PASP, 98, 635
Bock, D. C.-J., Large, M. I., & Sadler, E. M. 1999, AJ, 117, 1578
Boyle, B. J., Griffiths, R. E., Shanks, T., Stewart, G. C., & Georgantopoulos, I. 1993, MNRAS, 260, 49
Cartier, R., Lira, P., Coppi, P., et al. 2015, ApJ, 810, 164
Cioni, M.-R. L., Clementini, G., Girardi, L., et al. 2011, A&A, 527, A116
Cioni, M.-R. L., Kamath, D., Rubele, S., et al. 2013, A&A, 549, A29
Cioni, M.-R. L., Girardi, L., Moretti, M. I., et al. 2014, A&A, 562, A32
Cioni, M.-R. L., Bekki, K., Girardi, L., et al. 2015, ArXiv e-prints [arXiv:1510.07647]
Cross, N. J. G., Collins, R. S., Mann, R. G., et al. 2012, A&A, 548, A119
Dalton, G. B., Caldwell, M., Ward, A. K., et al. 2006, in SPIE Conf. Ser., 6269, 30
de Grijs, R., & Bono, G. 2015, AJ, 149, 179
DiPompeo, M. A., Bovy, J., Myers, A. D., & Lang, D. 2015, MNRAS, 452, 3124
Dobrzycki, A., Groot, P. J., Macri, L. M., & Stanek, K. Z. 2002, ApJ, 569, L15
Dobrzycki, A., Macri, L. M., Stanek, K. Z., & Groot, P. J. 2003a, AJ, 125, 1330
Dobrzycki, A., Stanek, K. Z., Macri, L. M., & Groot, P. J. 2003b, AJ, 126, 734
Dobrzycki, A., Eyer, L., Stanek, K. Z., & Macri, L. M. 2005, A&A, 442, 495
Emerson, J. P., Irwin, M. J., Lewis, J., et al. 2004, in SPIE Conf. Ser., 5493, 401
Emerson, J., McPherson, A., & Sutherland, W. 2006, The Messenger, 126, 41
Flesch, E. 2010, PASA, 27, 283
Gallastegui-Aizpun, U., & Sarajedini, V. L. 2014, MNRAS, 444, 3078
Geha, M., Alcock, C., Allsman, R. A., et al. 2003, AJ, 125, 1
Glikman, E., Urrutia, T., Lacy, M., et al. 2012, ApJ, 757, 51
Gordon, K. D., Meixner, M., Meade, M. R., et al. 2011, AJ, 142, 102
Gregg, M. D., Becker, R. H., White, R. L., et al. 1996, AJ, 112, 407
Gullieuszik, M., Groenewegen, M. A. T., Cioni, M.-R. L., et al. 2012, A&A, 537, A105
Hamuy, M., Walker, A. R., Suntzeff, N. B., et al. 1992, PASP, 104, 533
Hamuy, M., Suntzeff, N. B., Heathcote, S. R., et al. 1994, PASP, 106, 566
Hasinger, G., Burg, R., Giacconi, R., et al. 1998, A&A, 329, 482
Hook, I. M., McMahon, R. G., Boyle, B. J., & Irwin, M. J. 1994, MNRAS, 268, 305
Irwin, M. J., Lewis, J., Hodgkin, S., et al. 2004, in SPIE Conf. Ser., 5493, 411
Kerber, L. O., Girardi, L., Rubele, S., & Cioni, M.-R. 2009, A&A, 499, 697
Kozłowski, S., & Kochanek, C. S. 2009, ApJ, 701, 508
Kozłowski, S., Kochanek, C. S., & Udalski, A. 2011, ApJS, 194, 22
Kozłowski, S., Kochanek, C. S., Jacyszyn, A. M., et al. 2012, ApJ, 746, 27
Kozłowski, S., Onken, C. A., Kochanek, C. S., et al. 2013, ApJ, 775, 92
Lacy, M., Storrie-Lombardi, L. J., Sajina, A., et al. 2004, ApJS, 154, 166
Landoni, M., Falomo, R., Treves, A., et al. 2013, AJ, 145, 114
Li, C., de Grijs, R., Deng, L., et al. 2014, ApJ, 790, 35
Loaring, N. S., Dwelly, T., Page, M. J., et al. 2005, MNRAS, 362, 1371
Mauch, T., Murphy, T., Buttery, H. J., et al. 2003, MNRAS, 342, 1117
McConnachie, A. W. 2012, AJ, 144, 4
Miszalski, B., Napiwotzki, R., Cioni, M.-R. L., et al. 2011, A&A, 531, A157
Moehler, S., Modigliani, A., Freudling, W., et al. 2014a, The Messenger, 158, 16
Moehler, S., Modigliani, A., Freudling, W., et al. 2014b, A&A, 568, A9
Moretti, M. I., Clementini, G., Muraveva, T., et al. 2014, MNRAS, 437, 2702
Morrissey, P., Conrow, T., Barlow, T. A., et al. 2007, ApJS, 173, 682
Muraveva, T., Clementini, G., Maceroni, C., et al. 2014, MNRAS, 443, 432
Nandra, K., Laird, E. S., Adelberger, K., et al. 2005, MNRAS, 356, 568
Oke, J. B. 1990, AJ, 99, 1621
Peters, C. M., Richards, G. T., Myers, A. D., et al. 2015, ApJ, 811, 95
Piatti, A. E., Guandalini, R., Ivanov, V. D., et al. 2014, A&A, 570, A74

Piatti, A. E., de Grijs, R., Ripepi, V., et al. 2015a, MNRAS, 454, 839
Piatti, A. E., de Grijs, R., Rubele, S., et al. 2015b, MNRAS, 450, 552
Ripepi, V., Moretti, M. I., Clementini, G., et al. 2012a, Ap&SS, 341, 51
Ripepi, V., Moretti, M. I., Marconi, M., et al. 2012b, MNRAS, 424, 1807
Ripepi, V., Marconi, M., Moretti, M. I., et al. 2014, MNRAS, 437, 2307
Ripepi, V., Moretti, M. I., Marconi, M., et al. 2015, MNRAS, 446, 3034
Ross, N. P., Hamann, F., Zakamska, N. L., et al. 2015, MNRAS, 453, 3932
Rubele, S., Kerber, L., Girardi, L., et al. 2012, A&A, 537, A106
Rubele, S., Girardi, L., Kerber, L., et al. 2015, MNRAS, 449, 639
Shanks, T., Georgantopoulos, I., Stewart, G. C., et al. 1991, Nature, 353, 315
Shaya, E. J., Olling, R., & Mushotzky, R. 2015, AJ, 150, 188
Skrutskie, M. F., Cutri, R. M., Stiening, R., et al. 2003, VizieR Online Data Catalog: VII/233
Stern, D., Assef, R. J., Benford, D. J., et al. 2012, ApJ, 753, 30
Tatton, B. L., van Loon, J. T., Cioni, M.-R., et al. 2013, A&A, 554, A33
Tinney, C. G., Da Costa, G. S., & Zinnecker, H. 1997, MNRAS, 285, 111
van Loon, J. T., & Sansom, A. E. 2015, MNRAS, 453, 2341
Vanden Berk, D. E., Richards, G. T., Bauer, A., et al. 2001, AJ, 122, 549
Vanden Berk, D. E., Wilhite, B. C., Kron, R. G., et al. 2004, ApJ, 601, 692
Véron-Cetty, M.-P., & Véron, P. 2010, A&A, 518, A10
Voges, W., Aschenbach, B., Boller, T., et al. 1999, A&A, 349, 389
White, R. L., Becker, R. H., Gregg, M. D., et al. 2000, ApJS, 126, 133

Appendix A: Additional table and figures

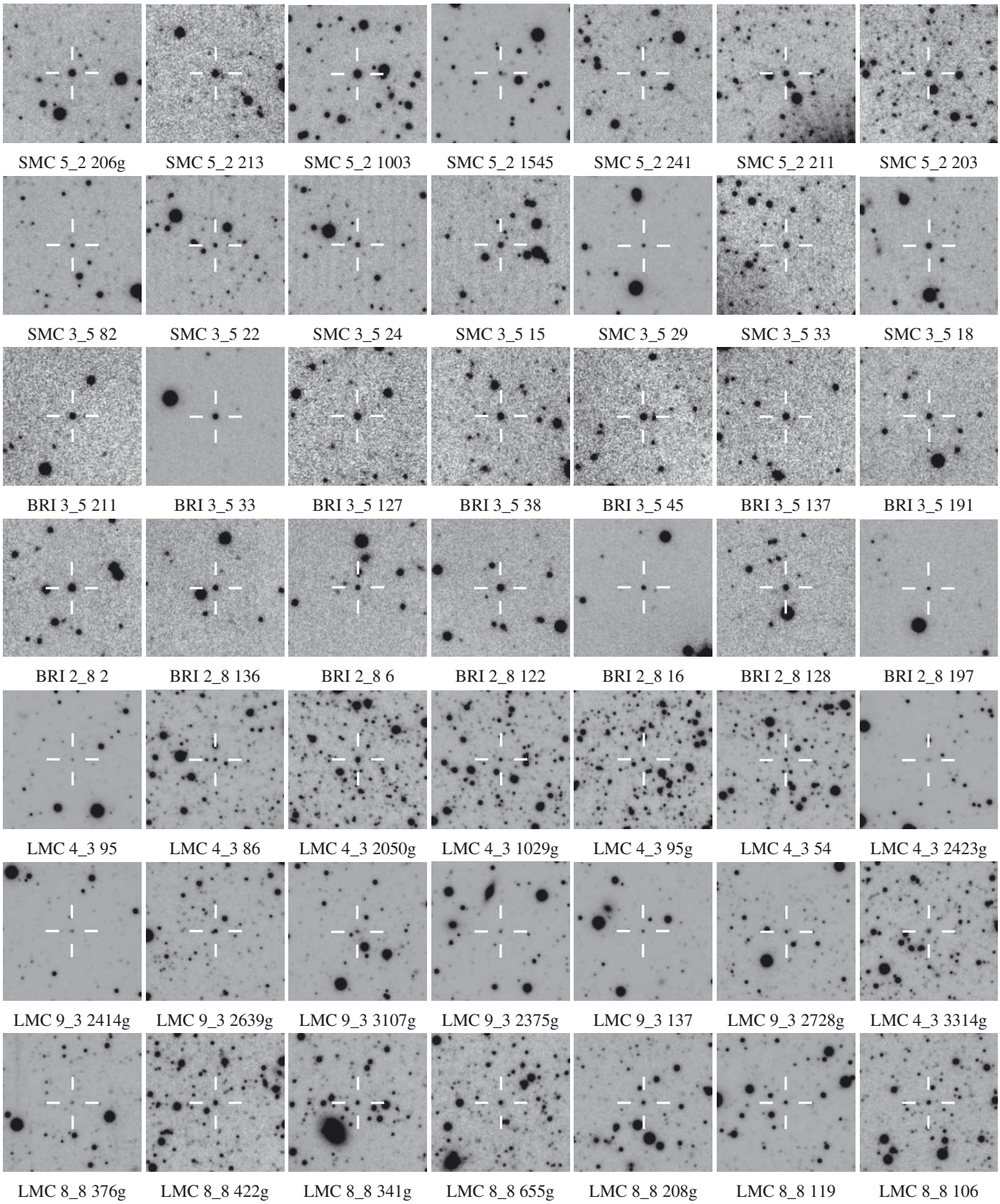

Fig. A.1. Finding charts in the *Y*-band for all 49 objects (crosses) with follow-up spectroscopy. The images are 1×1 arcmin^2. North is at the top and east is to the left.

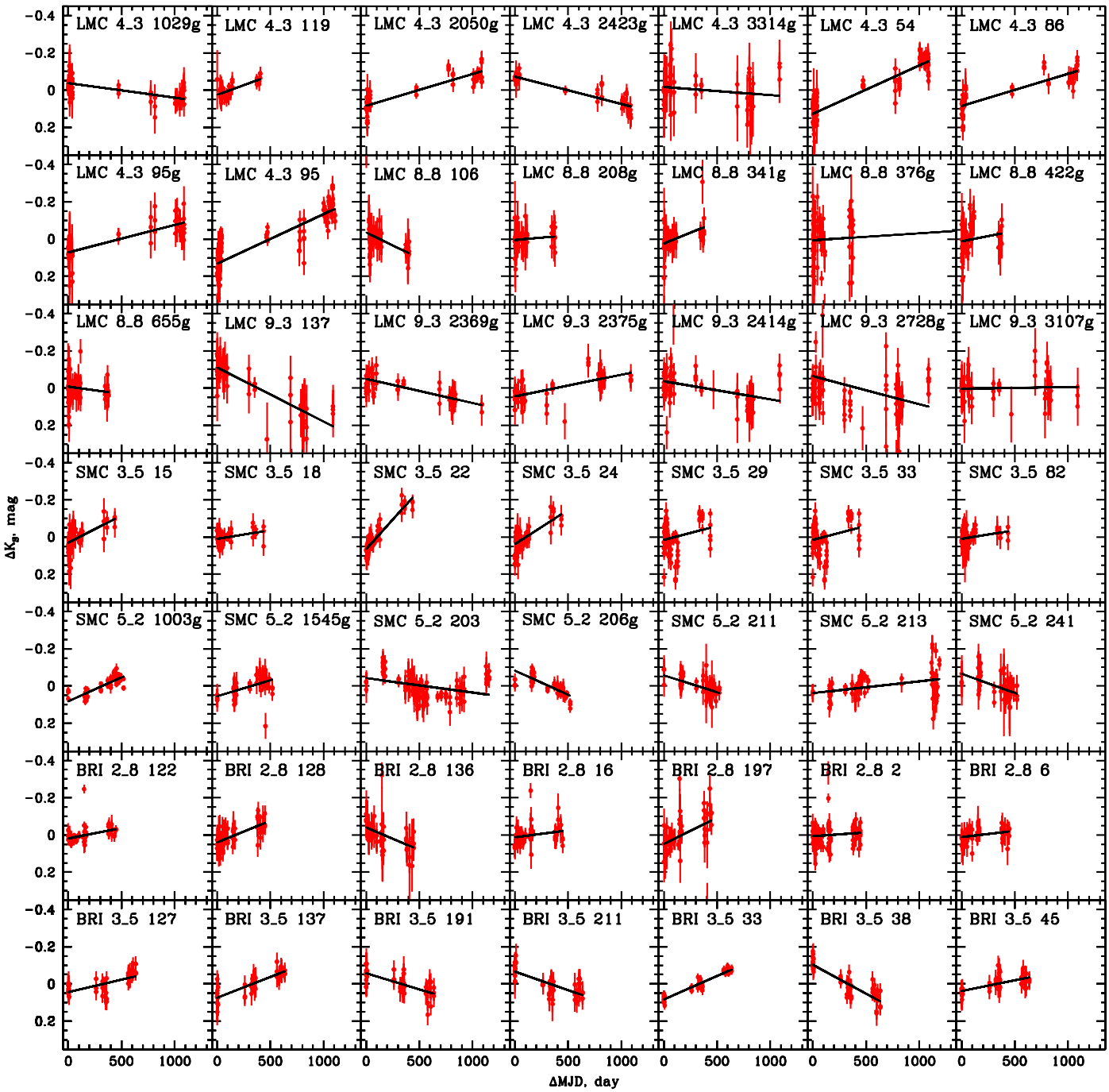

Fig. A.2. Light curves of the observed targets with their measurement errors as function of the time since the first available VMC observation. The lines show linear fits to the light curve, following Cioni et al. (2013).

Table A.1. Observing log for the spectroscopic observations.

Object ID	UT at start of obs. yyyy-mm-ddThh:mm:ss	Exp. (s)	sec z (dex)	Slit PA (deg)	Object ID	UT at start of obs. yyyy-mm-ddThh:mm:ss	Exp. (s)	sec z (dex)	Slit PA (deg)
SMC 5_2 206g	2013-09-19T03:03:02.918	450	1.564–1.553	39.420	BRI 2_8 128	2013-12-20T01:20:52.575	450	1.570–1.563	28.848
	2013-09-19T03:21:31.818	450	1.538–1.528	34.487		2013-12-20T01:29:06.984	450	1.563–1.557	28.848
	2013-09-19T03:38:04.857	450	1.518–1.510	28.975	BRI 2_8 197	2013-12-17T01:40:09.277	450	1.577–1.570	28.516
	2013-10-06T02:49:52.209	450	1.501–1.495	24.749		2013-12-17T01:48:23.554	450	1.571–1.565	28.516
SMC 5_2 213	2013-09-21T05:01:39.142	450	1.456–1.456	1.632	LMC 4_3 95	2013-12-16T01:45:37.003	450	1.553–1.542	41.352
	2013-09-21T05:09:52.905	450	1.457–1.458	1.632		2013-12-16T02:13:49.360	450	1.513–1.505	33.443
SMC 5_2 1003g	2013-09-19T04:31:02.937	450	1.477–1.474	15.682		2013-12-16T02:13:49.360	450	1.513–1.505	33.443
	2013-09-19T04:39:19.291	450	1.474–1.472	15.682	LMC 4_3 86	2013-12-06T03:52:04.763	450	1.481–1.477	17.331
	2013-09-19T04:48:49.290	900	1.469–1.466	15.682		2013-12-06T04:01:06.429	450	1.477–1.474	17.331
	2013-09-19T05:04:35.265	900	1.467–1.467	15.682	LMC 4_3 2050g	2013-12-06T06:38:59.929	450	1.584–1.595	−34.823
	2013-10-06T03:06:14.936	450	1.489–1.484	21.822		2013-12-06T07:00:31.052	450	1.620–1.634	−40.483
SMC 5_2 1545g	2013-10-06T02:01:51.030	450	1.570–1.559	43.242		2013-12-06T07:08:45.293	450	1.636–1.651	−40.483
	2013-10-06T02:01:51.030	450	1.582–1.570	43.242		2013-12-16T02:39:36.747	450	1.532–1.525	26.530
SMC 5_2 241	2013-09-21T05:25:18.826	450	1.467–1.469	−3.350		2013-12-16T02:47:53.185	450	1.525–1.519	26.530
	2013-09-21T05:33:33.959	450	1.470–1.472	−3.350	LMC 4_3 1029g	2013-12-14T02:43:41.008	450	1.515–1.507	28.440
SMC 5_2 211	2013-09-19T05:38:44.396	450	1.486–1.482	18.283		2013-12-14T02:52:53.409	450	1.507–1.500	28.440
	2013-09-21T04:47:22.625	450	1.476–1.474	10.386	LMC 4_3 95g	2013-12-06T07:36:29.244	450	1.663–1.682	−50.687
SMC 5_2 203	2013-10-06T02:30:32.040	450	1.554–1.533	35.887		2013-12-06T07:44:53.416	450	1.686–1.703	−50.687
	2013-09-19T05:38:44.396	900	1.474–1.478	−1.976		2013-12-17T02:10:00.512	450	1.528–1.518	36.054
SMC 3_5 82	2013-10-06T03:27:16.233	450	1.586–1.578	31.308		2013-12-17T02:18:16.740	450	1.518–1.510	36.054
	2013-10-06T03:35:32.467	450	1.579–1.571	31.308	LMC 4_3 54	2013-10-26T06:19:02.212	450	1.494–1.489	22.975
SMC 3_5 22	2013-10-06T03:52:07.075	450	1.553–1.547	23.025		2013-10-26T06:27:16.549	450	1.489–1.484	22.975
	2013-10-06T04:00:23.489	450	1.547–1.542	23.025	LMC 4_3 2423g	2013-12-06T06:07:31.796	450	1.539–1.548	−22.770
SMC 3_5 24	2013-10-19T01:28:36.091	450	1.684–1.669	56.651		2013-12-06T06:15:45.196	450	1.549–1.558	−22.770
	2013-10-19T01:36:50.388	450	1.669–1.655	56.651	LMC 9_3 2414g	2013-12-14T03:11:51.605	450	1.329–1.324	23.257
SMC 3_5 15	2013-09-21T05:49:00.250	450	1.577–1.570	28.516		2013-12-14T03:20:06.303	450	1.324–1.319	23.257
	2013-09-21T05:57:13.942	450	1.528–1.528	5.871	LMC 9_3 2639g	2013-12-14T03:46:35.555	450	1.314–1.312	15.528
SMC 3_5 29	2013-10-19T03:13:50.516	450	1.553–1.549	21.581		2013-12-14T03:54:49.053	450	1.312–1.311	15.528
	2013-10-19T03:13:50.516	450	1.558–1.553	21.581	LMC 9_3 3107g	2013-12-14T04:10:11.454	450	1.313–1.313	3.664
SMC 3_5 33	2013-10-19T02:25:32.964	450	1.612–1.602	37.230		2013-12-14T04:18:25.192	450	1.314–1.315	3.664
	2013-10-19T02:42:42.149	450	1.591–1.583	31.320	LMC 9_3 2375g	2013-12-02T06:53:48.740	450	1.391–1.403	−33.955
SMC 3_5 18	2013-10-19T01:58:05.902	450	1.629–1.617	45.531		2013-12-02T07:02:03.233	450	1.405–1.418	−33.955
	2013-10-19T01:58:05.902	450	1.642–1.629	45.531	LMC 9_3 137	2013-10-24T08:19:21.576	450	1.311–1.315	−10.420
BRI 3_5 211	2013-10-19T03:40:13.964	450	1.592–1.581	39.917		2013-10-24T08:27:35.722	450	1.316–1.322	−10.420
	2013-10-19T03:48:28.241	450	1.581–1.570	39.917		2013-12-14T05:09:17.236	450	1.318–1.324	−14.550
BRI 3_5 33	2013-09-19T06:24:35.926	900	1.551–1.538	28.379		2013-12-14T05:01:02.359	450	1.312–1.317	−14.550
	2013-10-25T05:33:21.894	450	1.515–1.516	−0.353	LMC 9_3 2728g	2013-12-14T04:38:39.096	450	1.314–1.317	−5.871
BRI 3_5 127	2013-10-25T05:08:18.317	450	1.508–1.507	6.722		2013-12-14T04:46:53.124	450	1.318–1.321	−5.871
	2013-10-25T05:16:33.912	450	1.508–1.508	6.722	LMC 9_3 3314g	2013-12-14T05:23:37.461	450	1.340–1.347	−20.100
BRI 3_5 38	2013-10-25T04:05:06.336	450	1.550–1.544	26.542		2013-12-14T05:31:52.118	450	1.348–1.355	−20.100
	2013-10-25T04:13:22.532	450	1.544–1.538	26.542	LMC 8_8 376g	2013-12-16T03:06:48.200	450	1.405–1.394	39.568
BRI 3_5 45	2013-10-25T04:28:37.857	450	1.541–1.536	19.587		2013-12-16T03:15:03.097	450	1.394–1.384	39.568
	2013-10-25T04:37:23.194	450	1.536–1.532	19.587	LMC 8_8 422g	2013-12-17T02:35:54.490	450	1.453–1.439	45.899
	2013-10-25T04:53:49.615	450	1.529–1.526	11.984		2013-12-17T02:44:22.309	450	1.438–1.425	45.899
BRI 3_5 137	2013-12-06T00:59:03.176	450	1.563–1.546	35.864	LMC 8_8 341g	2013-12-16T03:30:52.459	450	1.374–1.366	32.171
	2013-12-06T01:24:09.790	450	1.537–1.524	25.592		2013-12-16T03:30:52.459	450	1.374–1.366	32.171
BRI 3_5 191	2013-12-06T02:26:38.545	450	1.496–1.494	9.317	LMC 8_8 655g	2013-12-16T03:06:48.200	450	1.376–1.368	32.215
	2013-12-06T02:35:23.131	450	1.495–1.495	9.317		2013-12-18T03:34:26.078	450	1.368–1.361	32.215
BRI 2_8 2	2013-12-16T00:52:43.405	450	1.606–1.596	38.691	LMC 8_8 208g	2013-12-02T08:13:39.103	450	1.448–1.463	−41.914
	2013-12-16T01:00:59.222	450	1.596–1.586	38.691		2013-12-02T08:21:52.875	450	1.465–1.481	−41.914
BRI 2_8 136	2013-12-16T01:19:26.655	450	1.572–1.564	31.100	LMC 8_8 119	2013-12-02T07:22:06.873	450	1.397–1.405	−23.932
	2013-12-16T01:27:42.032	450	1.564–1.557	31.100		2013-12-02T07:30:21.006	450	1.407–1.416	−23.932
BRI 2_8 6	2013-12-17T01:11:07.305	450	1.573–1.564	32.348	LMC 8_8 106	2013-12-06T08:02:27.464	450	1.459–1.475	−42.992
	2013-12-17T01:19:23.793	450	1.564–1.557	32.348		2013-12-06T08:10:42.015	450	1.477–1.493	−42.992
BRI 2_8 122	2013-10-25T06:14:04.428	450	1.516–1.516	13.588		2013-12-17T03:00:19.702	450	1.425–1.413	41.905
	2013-10-25T06:36:35.734	450	1.517–1.519	−0.962		2013-12-17T03:08:34.649	450	1.413–1.402	41.905
BRI 2_8 16	2013-10-25T05:50:24.517	450	1.549–1.547	13.588					
	2013-10-25T05:58:38.992	450	1.547–1.544	13.588					

Notes. Starting times, exposure times, starting and ending airmasses, and slit position angles for each exposure are listed on separate successive lines.